Physica D 292–293 (2015) 62–69

Contents lists available at ScienceDirect

Physica D

journal homepage: www.elsevier.com/locate/physd

Instability observations associated with wave breaking in the stable-stratified deep-ocean

Hans van Haren

Royal Netherlands Institute for Sea Research (NIOZ), P.O. Box 59, 1790 AB Den Burg, the Netherlands

HIGHLIGHTS

- Rare Rayleigh–Taylor instabilities in stable-stratified ocean conditions.
- Instabilities induced by internal wave motions overcoming reduced gravity.
- Sufficient condition for overall instability.
- Efficient near-bottom mixing.

ARTICLE INFO

Article history:
Received 18 March 2014
Received in revised form
28 October 2014
Accepted 7 November 2014
Available online 15 November 2014
Communicated by H.A. Dijkstra

Keywords:
High-resolution temperature observations
Breaking internal waves
Rayleigh–Taylor instabilities in stable stratification
Deep-ocean topography

ABSTRACT

High-resolution temperature observations above underwater topography in the deep, stably stratified ocean have revealed two distinctive turbulence processes. These processes are associated with different phases of a large-scale (here tidal) internal gravity wave: (i) highly nonlinear turbulent bores during the upslope propagating phase, and (ii) Kelvin–Helmholtz billows, at some distance above the slope, during the downslope phase. Whilst the former may be associated in part with convective turbulent overturning following Rayleigh–Taylor instabilities 'RTi', the latter is mainly related to shear-induced Kelvin–Helmholtz instabilities. In this paper, details are particularly presented of rare (convective) RTi penetrating stable density stratification under high-frequency internal waves. Such 'apparent RTi' can be explained using both stability parameterization of entrainment across a density interface, and, more relevant here, internal wave acceleration overcoming the reduced gravity.

1. Introduction

In nonlinear fluid dynamics, Rayleigh–Taylor instability RTi is the basis of an important turbulence exchange mechanism across an interface between two fluids of different densities that occurs when the less dense fluid is accelerated into the other [1,2]. The initial finger-like penetrations of fluid grow into 2D-mushrooms and eventually generate full-3D turbulence. It is a quite efficient way of turbulent mixing, with efficiencies between 0.25 and 0.5, the maximum, as determined from laboratory experiments [3]. In such experiments, basically two methods exist generating RTi: one is to fill a container with a stably stratified (usually two-layer) fluid and turn the container rapidly upside-down (e.g., [4]) or accelerate it downward by more than 1G (e.g., [5]); a second is to fill a container with an unstable stratified fluid separating the two layers of different densities by a plate and pull the plate away smoothly (e.g., [6]). Outside the laboratory environment, the RTi-induced mixing mechanism is important in many geophysical environments. For example, during day-time the atmosphere is heated from below so that RTi can act under gravity, warm air being less dense than cold air, resulting in strong vertical turbulent motions [7]. In case of stably stratified air above, such RTi may generate 'internal waves' [8].

In geophysics, RTi is often termed 'convective' or 'free' instability to distinguish it from vertical current differences (shear)-induced Kelvin–Helmholtz instability (KHi). In its initial stage, KHi consists of thin layers of different densities rolled-up by the vertical current difference 'shear' across the initial stable density interface (Fig. 1(b)). It is thus more associated with stable density-stratified environments, like the ocean that is generally heated from above. In that largest natural body of fluid, shear-induced turbulence reaches a mean mixing efficiency of about 0.2, at least in the upper layers [9].

In the ocean, RTi is mainly associated with dense-water-formation during periods of near-surface drying and cooling in the polar regions and the Mediterranean, but also more wide-spread in the first 10–20 m below the surface during night-time cooling. In the stratified deep-ocean, no detailed observations have been

E-mail address: hans.van.haren@nioz.nl.

http://dx.doi.org/10.1016/j.physd.2014.11.002
0167-2789/

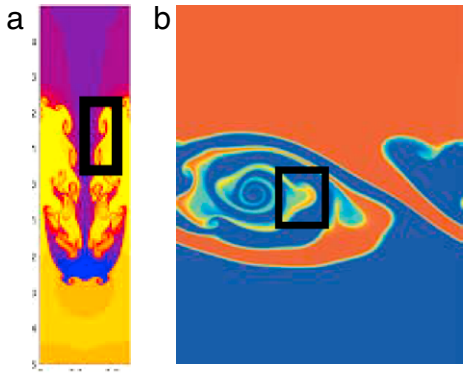

Fig. 1. Examples of numerical modeling studies of particular stages of instability developments. (a) One finger of Rayleigh–Taylor instability in semi-full turbulence stage, with secondary Kelvin–Helmholtz instability along its penetrative fringe in the black rectangle (from: [10]). (b) Roll-up stage of Kelvin–Helmholtz instability becoming turbulent with secondary Rayleigh–Taylor instability mushroom emerging in the black rectangle (from: [11]).

made of RTi thus far. However, the stable density stratification can support internal (inertia-gravity) waves that set the ocean interior in permanent motion. Most of their energy comes from passing atmospheric disturbances near the surface or from tidal currents interacting with ubiquitous seafloor topography. Wave–topography interaction and wave–wave interactions transfer energy from large-scale sinusoidal linear waves to highly nonlinear waves that can break, foremost at underwater topography. Here, the variable turbulence generation is demonstrated of internal wave breaking observations. High-resolution temperature sensors also reveal details of apparent RTi-penetration in stably stratified layering underneath high-frequency internal waves near the buoyancy frequency, the upper limit of free-propagating internal waves.

From laboratory experiments and numerical modeling efforts we know that the above two types of instabilities can occur co-jointly (Fig. 1). Matsumoto and Hoshino [11] demonstrated the mushroom formation stage of RTi occurring and accelerating turbulent mixing in the interior of well rolled-up billows after initial-stage KHi. It can be expected that this RTi-portion inside KHi increases the mixing efficiency of KHi. As the roll-up stage consists of alternating stable and unstable density layering under gravity, KHi rapidly transfers to a fully turbulent billow core that is convectively RTi-driven [12]. Conversely during the third stage of RTi, small-scale KHi develops on the sharp interfaces between larger-scale columns of fluids of different densities being moved up and down (Fig. 1(a)). As these small-scale KHi are at the density interface, their mixing efficiency, and thus the vertical density flux, will be high as well.

An important parameter in laboratory studies of RTi is the Atwood number $A = \Delta\rho/\Sigma\rho$, the ratio of the density (ρ) difference across an interface and the sum of the different densities. At small (positive) Atwood numbers $0 < A \ll 1$, instabilities show a symmetric start of instability [3,13]; the flow is considered a Boussinesq flow. In the developed stage, no KHi is observed along the edges and the growth rates of turbulence and interface thickening are slow [3,4]. In laboratory experiments, small (positive) $A \sim 10^{-3}$. It is noted that in the present ocean observations $A \sim -10^{-5}$, and thus is very small compared to laboratory experiments (and negative, for stable stratified conditions).

A key parameter for flows under stable stratified conditions is the (overall) Richardson number $\mathrm{Ri} = g\Delta\rho/\rho \cdot \Delta z/V^2$, in which g denotes the acceleration of gravity, Δz a suitable vertical length-scale such as the interface thickness and V the current speed (difference across it). Ri thus represents the ratio of stability (by the stratification) over the destabilizing (shear-) flow, or the ratio of potential over kinetic energy. In the latter context, the current speed may represent turbulent motions in one or both layers, and in which case a dependence of penetration velocity w_e across the interface may be formulated [14]. From Turner's laboratory experiments it is found that $w_e/V \sim \mathrm{Ri}^{-1}$, up to about $\mathrm{Ri} = 0.25$, the limit of linear stability as formulated by [15,16]. Later experiments by [6] showed more or less the same dependence, $\sim \mathrm{Ri}^{-1.3}$. It is noted that time-dependent nonlinear flows as in 3D internal waves may exhibit instabilities at $\mathrm{Ri} = 1$ [17,18] or even $\mathrm{Ri} > 1$ [19]. However, little observational evidence exists for the latter theoretical results.

So far, limited KHi has been observed directly in natural waters, notable exceptions being by, e.g., [20–23]. Few show the stage of roll-up [20,24], and mostly the state of collapse into a billow with a fully turbulent core ([22,25]; the present observations). In laboratory experiments, it takes only seconds to transfer from the initial roll-up to the full turbulence stage [12]. This may be slower in natural waters like the ocean, but even there statistics predict it to be (much) less observed than a fully turbulent billow in different stages of matureness.

2. Data

The present observations have been made in the NE-Atlantic Ocean at depths well-above the Mediterranean outflow of salty and warm waters that have a density equivalent to that of the Atlantic Ocean between 800 and 1300 m. A bottom-lander with a net weight of 200 kg was moored at 30° 00.052′N, 28° 18.802′W, $H = 549$ m water depth, near the top of the eastern slope of Great Meteor Seamount in the Canary Basin for 18 days in May/June 2006. The lander held a 300 kHz four-beam Teledyne/RDI acoustic Doppler current profiler 'ADCP' and an SBE53 high-precision pressure sensor. Attached to the lander was a nylon-coated steel mooring cable below a single elliptic underwater buoy. We taped 98 custom-made 'NIOZ3' temperature sensors to the cable at 0.5 m intervals. The lander held 3 additional sensors, so that the lowest sensor was nominally at 0.5 m from the bottom. Tilt and pressure data from sensors just below the buoy showed that the top of the mooring line moved less than 0.15 m vertically and less than 3.5 m horizontally.

The NIOZ3 sensors sampled at a rate of 1 Hz and were synchronized via induction every 4 h, so that timing mismatch was <0.02 s. Their noise level is $<6 \times 10^{-5}$ °C [26]. The frame's pressure sensor sampled at a rate of 0.333 Hz and showed random sampling errors <4 Nm^{-2} [27]. The ADCP sampled at a rate of 0.5 Hz, registering all three Cartesian current components $[u, v, w]$ and, in each beam, echo intensity every 1 m between 5 and 84 m above the bottom. The acoustic echo, taken relative to the time mean to correct for the water attenuation of sound, is most sensitive to suspended particles and especially zooplankton (small shrimp) having sizes >0.003 m [28]. At 300 kHz, zooplankton reflects sound approximately at the level of strong turbulence, e.g., caused by breaking internal waves [29]. This level is about 20 dB above that of weak turbulence, say the background level of relative echo intensity. Unfortunately, the ADCP-data were rather noisy due to regular lack of scatterers in combination with occasional hard reflectance at the titanium housings of the temperature sensors.

Shipborne SeaBird-911 Conductivity–Temperature–Depth 'CTD'-profiles demonstrated that the local stable density stratification $d\rho/dz$ amounted $N = 3.2 \pm 1.5 \times 10^{-3}$ s^{-1} in terms of buoyancy frequency $N \propto (-g/\rho d\rho/dz)^{1/2}$ + compressibility effects. This resulted in an average internal wave slope of 1.5° at the semidiurnal tidal frequency, so that the local bottom slope of 3.5 ± 0.5° was significantly super-critical for internal tides [30].

Temperature sensor data are first transferred to conservative (~potential) temperature (Θ) values [31], before they are used as a tracer for potential density variations $\delta\rho$ following a constant linear relationship obtained from best-fit data using the nearby

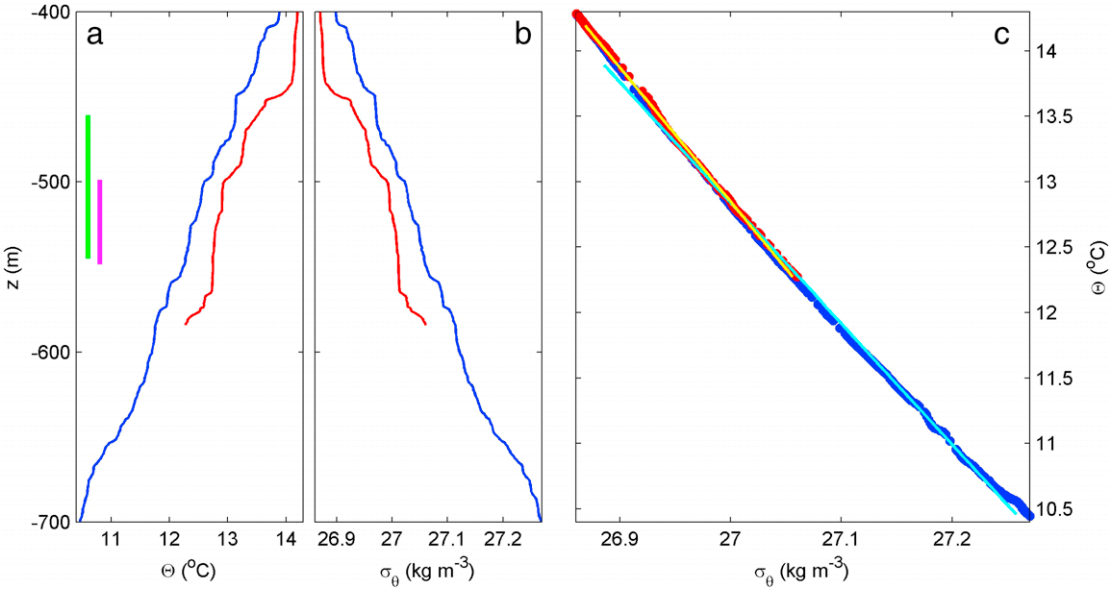

Fig. 2. Overview of CTD-data obtained at 1 (red) and 5 km (blue) east of the mooring site, immediately before deployment. a. Conservative temperature. The vertical bars indicate the ranges of the moored temperature (purple) and ADCP current measurements (green). b. Potential density anomaly, referenced to the surface. c. Potential density anomaly—conservative temperature relationship. The straight lines (yellow for red; light-blue for blue) are linear best-fits to the sections of data presented, resulting in a mean relationships of $\delta\sigma_\theta = -0.103 \pm 0.005\delta\Theta$ kg m^{-3}. (For interpretation of the references to color in this figure legend, the reader is referred to the web version of this article.)

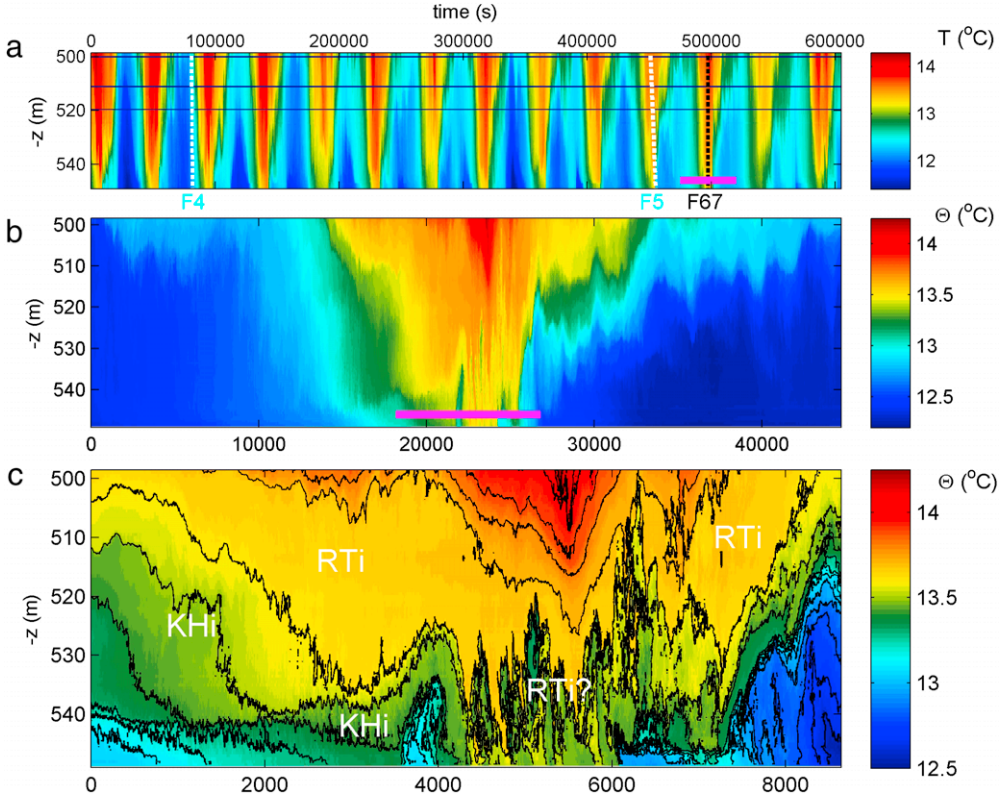

Fig. 3. High-resolution moored temperature observations above Great Meteor Seamount. (a) One week of depth-time series of original temperature after calibration; the horizontal lines indicate missing sensor data. The purple bar indicates the period of panel b; the vertical white dashed lines indicate the periods of Figs. 4 ('F4') and 5 ('F5'); the vertical black dashed line indicates the period of panel c and Figs. 6, 7 ('F67'). (b) One semidiurnal lunar tidal period from panel a, whereas missing sensor data are interpolated and measured temperature is transferred to conservative temperature; the purple bar indicates the period of panel c. (c) One-sixth tidal period from panel b, demonstrating the warming phase of a tidal period, a high-frequency internal wave and various instabilities. Solid-black contours are drawn every 0.1 °C. (For interpretation of the references to color in this figure legend, the reader is referred to the web version of this article.)

CTD-profiles across 300 m vertically, six times the range of the temperature sensors. This provides an indication for the variability of water mass properties over the large vertical ($\Delta z \sim 100$ m) buoyancy and internal tidal wave scales. The amount of sensors and the 0.5 m-resolution of the small buoyancy scales are sufficient to use these data to estimate turbulence parameters. These

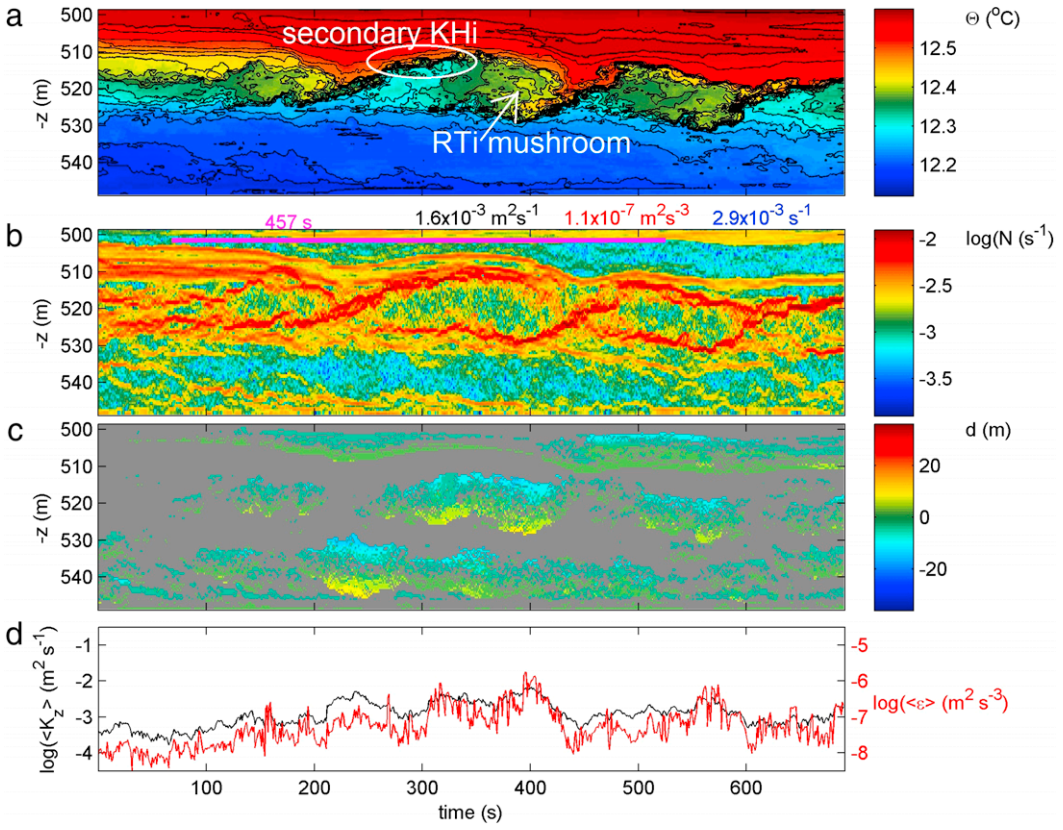

Fig. 4. Detail depth-time (11.5 min) series of a small train of 20 m high KHi billows during a warming, downslope moving phase of the tide. The KHi shows secondary instabilities in the form of small-KHi along the rims and some mushroom RTi in the interior. (a) Conservative temperature; solid-black contours are drawn every 0.025 °C. (b) Logarithm of the buoyancy frequency, computed from reordered, statically stable conservative temperature data. In purple (and bar length) the time-depth-maximum buoyancy period $2\pi/N_{\max}$ is indicated; in black time-depth-mean turbulent diffusivity $[\langle K_z\rangle]$; in red turbulence dissipation rate $[\langle\varepsilon\rangle]$; in blue buoyancy frequency $[\langle N\rangle]$. (c) Displacements of the reordering. (d) Time series of the logarithm of vertically averaged turbulence dissipation rate ($\langle\varepsilon\rangle$; red; scale to right) and turbulent diffusivity ($\langle K_z\rangle$; black). (For interpretation of the references to color in this figure legend, the reader is referred to the web version of this article.)

estimates are not made via resolution of the smallest Kolmogorov-scales $O(10^{-3} - 10^{-2})$ m of turbulence dissipation, but through the resolution of scales of up to the largest energy-containing Ozmidov-scales of turbulence in stratified fluids.

Thus, turbulent kinetic energy dissipation rate $\varepsilon = C_0^2 d^2 N^3$, $C_0 = 0.8$ a constant, and vertical (z) turbulent eddy diffusivity $K_z = \Gamma\varepsilon N^{-2} = 0.128 d^2 N$, Γ the mixing efficiency coefficient, are estimated by calculating 'overturning' scales d after reordering every 1 Hz time-step the potential density (temperature) profile, which may contain inversions, into a stable monotonic profile without inversions [32,33]. The value of $C_0 = 0.8$ was found to be the mean with values varying over one order of magnitude after a comparison between overturning and Ozmidov scales [34,35]. Here, a constant, mean mixing efficiency of $\Gamma = 0.2$ is used, which is common under shear-induced turbulent stratified-ocean conditions [9,36,37], although debate is ongoing as it may be variable with space and time under particular conditions (e.g., [38]). As the noise level of the temperature sensors is very low, the threshold for detecting overturns is mainly due to remaining temperature-shifts after calibration ($<5 \times 10^{-4}$ °C; [26,30]).

In the following, averaging over time is denoted by $[\ldots]$, averaging over depth-range by $\langle\cdots\rangle$. The specific averaging periods and ranges are indicated with the mean values.

3. Observations

Between 400 and 700 m above the slopes of Great Meteor Seamount, the temperature–density relationship is reasonably tight $\delta\rho = \alpha\delta\Theta, \alpha = -0.103 \pm 0.005$ kg m^{-3} °C^{-1} (Fig. 2). Repeated CTD-observations show very little variation in this relationship, and the effects of salt-compensated intrusions are confirmed negligible. As a result, the temperature sensor observations can be used as a tracer for density variations and estimates of turbulence parameters.

A one-week portion of the moored Eulerian temperature observations show an apparently regular variation with the semidiurnal periodicity, of alternating warm (upper layer; colored red) and cool (lower layer; blue) waters (Fig. 3(a)). The 50 m high range of the 101 sensors does not resolve the entire amplitude of the tidal, large-scale internal waves, which are estimated about 100 m (from the yellow–green 'contour'), crest–trough. In detail, none of the semidiurnal tidal periods are the same, with varying temperature fluctuations, intensity of high-frequency internal waves, influence of nonlinearity and turbulence generation.

In a one-tidal-period example (Fig. 3(b)), high-frequency 'smaller scale' internal waves near the buoyancy frequency are seen to accompany the large-scale variation. The smaller-scale internal waves have amplitudes of about 10 m and are generally resolved by the sensors' range. The warming downslope-moving phase of the internal tidal wave has an apparent smoother character than the cooling upslope-moving phase. The former is characterized by shear-induced KHi [25] or asymmetric Holmboe instability [39] at the main interface that descends with time; the latter is characterized by a highly nonlinear frontal bore or backwards breaking wave, of which the particle velocity is close to the phase speed, that is preceded by convective overturning RTi in the large near-homogeneous interior layer above the

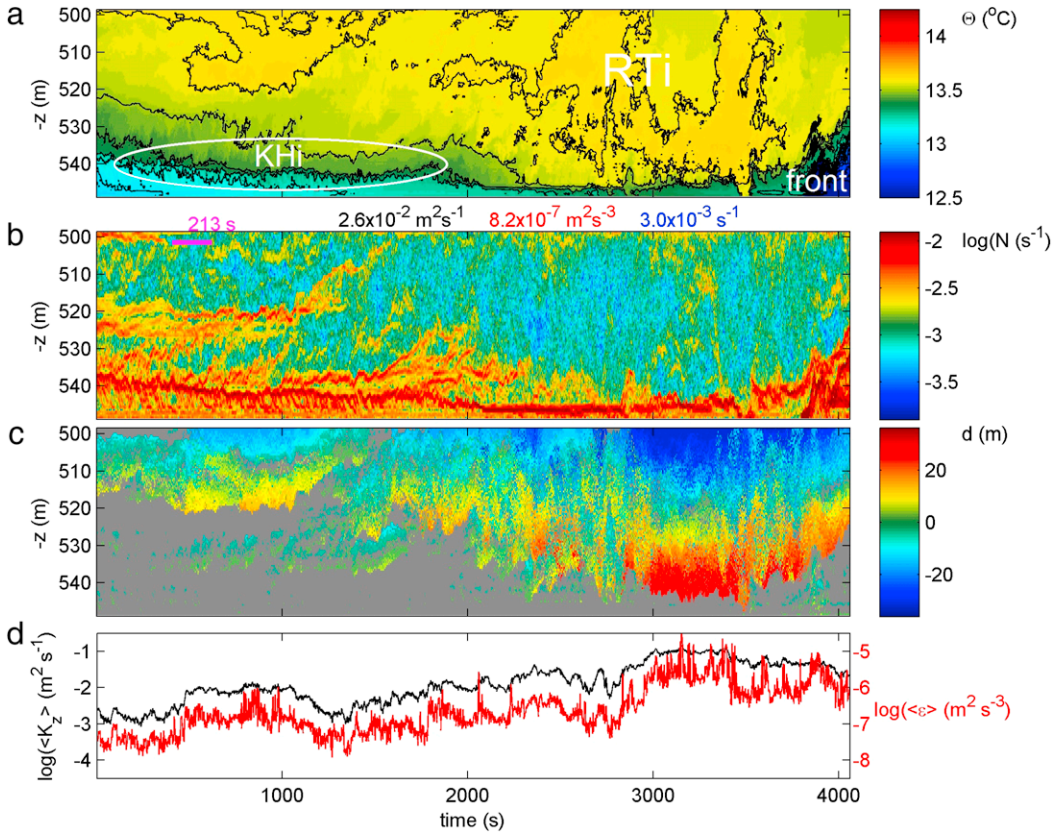

Fig. 5. As Fig. 4, but for 1.12 h period of observations just before the turn of tide from warming, downslope to cooling, upslope motion. This hour of downdraft is dominated by RTi in the weakly stratified layer above a strongly stratified interface just above the bottom. When the interface is still more than 5 m above the bottom, small KHi billows are visible below it. Colors and scales are identical to those in Fig. 6. (For interpretation of the references to color in this figure legend, the reader is referred to the web version of this article.)

strong stratification close to the bottom [30]. Both main types of turbulence generation exist in the details of Fig. 3(c), see several named indicators. Special there is the apparent-RTi 'RTi?' below the warmest portion of descending wave, and which seems to create convective overturning in rather strongly stratified waters below, with the 20 m high convective motions touching the bottom. Before these are discussed further, some examples of more classic KHi and RTi are treated first.

3.1. Occasional RTi in developed KHi

During the warming downslope moving phase of the tide, trains of Kelvin–Helmholtz billows are regularly observed (examples in [25] and Fig. 4 here). Classic roll-up of thin-layer stratification is not found in any of our temperature sensor observations so far. Although the rims of the present KHi consist of thin layers of enhanced stratification, the billows, like observed asymmetric Holmboe overturns [39], are always found in their late-stage of fully (convective) turbulence development. In this stage, only occasionally mushroom RTi-initial stages are observed (arrow in Fig. 4(a) near 390 s; 520 m). More often, small-scale billow-overturns are observed, also in the thin-layer rim. The latter provides relatively high mixing efficiency, or a large flux. When such cases dominate, the vertically averaged estimates of turbulence dissipation rate (Fig. 4(d) red graph; ∼ vertical heat flux) are relatively large compared with those of eddy diffusivity (Fig. 4(d) black graph). This is because the $\langle K_z \rangle$ is less dependent on N, so that it can attain high values in weakly stratified layers.

Relatively large $\langle K_z \rangle$, compared with $\langle \varepsilon \rangle$ and heat flux, is often found in weakly stratified and strongly turbulent layers associated with the final part of the warming downslope moving phase of the tide, see for an example Fig. 5. This highly RTi-dominated period consists of overturns exceeding 40 m in height and which are thought to sharpen the following frontal transition to the cooling upslope moving phase [30]. Together with the frontal passage (of which the beginning is shown in the lower-right corner in Fig. 5(a)), this is the most vigorous turbulence portion in a tidal period. They contribute about 60% of the total tidal period turbulence in half an hour [30]. The well-developed turbulence creates a several 10's of meters thick near-homogeneous layer that does not reach the bottom, normally. Below it, a thin strongly stratified layer is pushed to within a few m from the bottom. This stratified layer contains KHi (below it) when it is still about 10 m above the bottom (left-third portion around 540 m of Fig. 5(a), also visible in the oblique loops in stratification Fig. 5(b); see Fig. 4(b) for reference). These KHi become increasingly squashed over time by the RTi above and the approaching bottom below in the second half of the period.

3.2. Apparent-RTi in stably stratified waters underneath high-frequency internal waves

An unusual period of apparent RTi in a well-stratified layer is observed once around the transition from a warming downslope-moving to a cooling upslope-moving phase of the internal tide (Figs. 6, 7). During this period, relatively large $\langle \varepsilon \rangle$ is observed, compared with $\langle K_z \rangle$, while overall mean turbulence parameter values are (just) slightly less than during the comparable phase of the tidal period before (Fig. 5). The higher mixing efficiency in Figs. 6, 7 is comparable to that of the vertical heat flux associated with KHi-thin layer overturning. Initially, the warming downslope-moving phase still has a 'normal' apparition, with KHi between 530 and 540 m, and larger overturns due to RTi higher-up in a

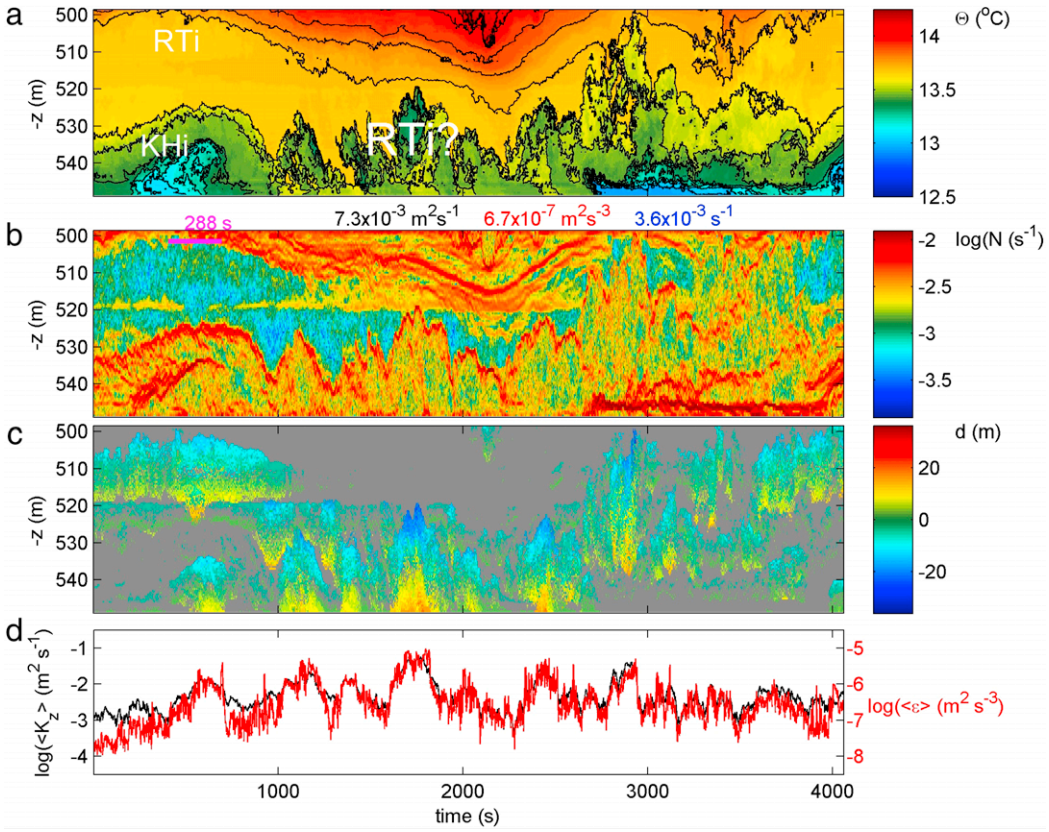

Fig. 6. As Fig. 4, but for 1.12 h period of observations from Fig. 2(c), dominated by apparent RTi underneath an internal wave near the buoyancy frequency. Colors and scales are identical to those in Fig. 5. (For interpretation of the references to color in this figure legend, the reader is referred to the web version of this article.)

weakly stratified layer between 510 and 530 m (Fig. 6). In contrast with other tidal periods however, a pre-frontal upslope-moving near-bottom motion pushes cooler water upwards around 500 s. In the 3000 s thereafter, and underneath the warmest water moving down in a high-frequency internal wave having a period close to the mean buoyancy period, short-scale 'fingers' occur: 'RTi?'. The fingers penetrate the 20 m-thick near-homogeneous layer of RTi (that was pushed down by the short internal wave) on their upper side, and the previous KHi-dominated 10 m-thick weakly stratified layer on their lower side. The associated turbulent overturns reach the bottom, a rare phenomenon for the warming downslope-moving tidal phase, and up to 30 m above it. They have duration of 250–300 s, close to the shortest buoyancy period of the strongest thin-layer stratification (the minimum period of 288 s here is indicated in purple in Fig. 6(b)). This is also the time-scale of variation of vertically averaged turbulence parameters (Fig. 6(d)). The structure of the fingers resembles RTi (Fig. 1(a)), with pointed shapes downward-oriented and rounded ones upward, except that they appear to occur in (overall) stable stratification. It would work when Fig. 6(a) is held upside-down. Or, when the wave-acceleration overcomes gravity, in this case gravity associated with density differences (see discussion in Section 4).

The associated vertical currents reach speeds of 0.06 m s^{-1}, down and up (Fig. 7(b)). Two large-scale variations of one down and one up dominate the motions in this figure. These are associated with the buoyancy-period internal wave. The $O(10$ m) horizontally averaged currents do not resolve much of the small-scale motions associated with the overturns, with exceptions around 2000 s near the bottom. It implies the turbulent motions have horizontal scales smaller than 10 m. This is confirmed by the observations on relative echo intensity that is measured in the $O(1$ m) wide individual acoustic beams, and of which two depth-time series are shown in Fig. 7(c), (d). Especially in the lower 20 m above the bottom, variations in echo intensity match well with variations in temperature (Fig. 7(a)) that are associated with the finger-like overturns. Between the two acoustic beams it is seen that the forms of echo intensity-variations shift in time, by typically 30–100 s (the 288 s purple bar of minimum buoyancy period can be used for reference). As the beams are spread by about 10 m horizontally, this time-shift associates with the advective horizontal current plus wave propagation speed $O(0.1$ m $s^{-1})$.

The downslope horizontal current component of >0.25 m s^{-1} is found around 500 m, which is unusually far, between 30 and 40 m, above the bottom (Fig. 7(e)). It reaches maximum speed in the core of the buoyancy period internal wave (red color in temperature in Fig. 7(a)), just prior to the transition from warming to cooling tidal phase. The core of the horizontal current and the zone of most intense apparent penetrative RTi are accompanied by strongly enhanced values of acoustic echo intensity (Fig. 7(c), (d)). Therein, two separate sets can be distinguished, the largest (red–brown; saturated values) is found in the interior, whilst the smaller one is confined to the bottom and directly reflects resuspension of sediment by the turbulence activity.

The turbulence activity associated with internal wave breaking is also registered in the bottom pressure sensor (purple graph in Fig. 7(g)). As demonstrated more elaborately in [27], the extensive turbulence above a sloping bottom provides a rather continual activity in bottom pressure that is often mistakenly attributed to long surface waves (e.g., [40]). Using temperature observations, even though limited in the lower 50 m above the bottom only, and vertical current information, observed bottom pressure is seen to be dominated by two terms: the internal hydrostatic pressure (black graph in Fig. 7(g)) and non-hydrostatic pressure (red). The former reflects the slower pressure effects due to internal waves near the buoyancy frequency, whilst the latter reflects the shorter time-scale, mainly turbulence variations. Added together, they

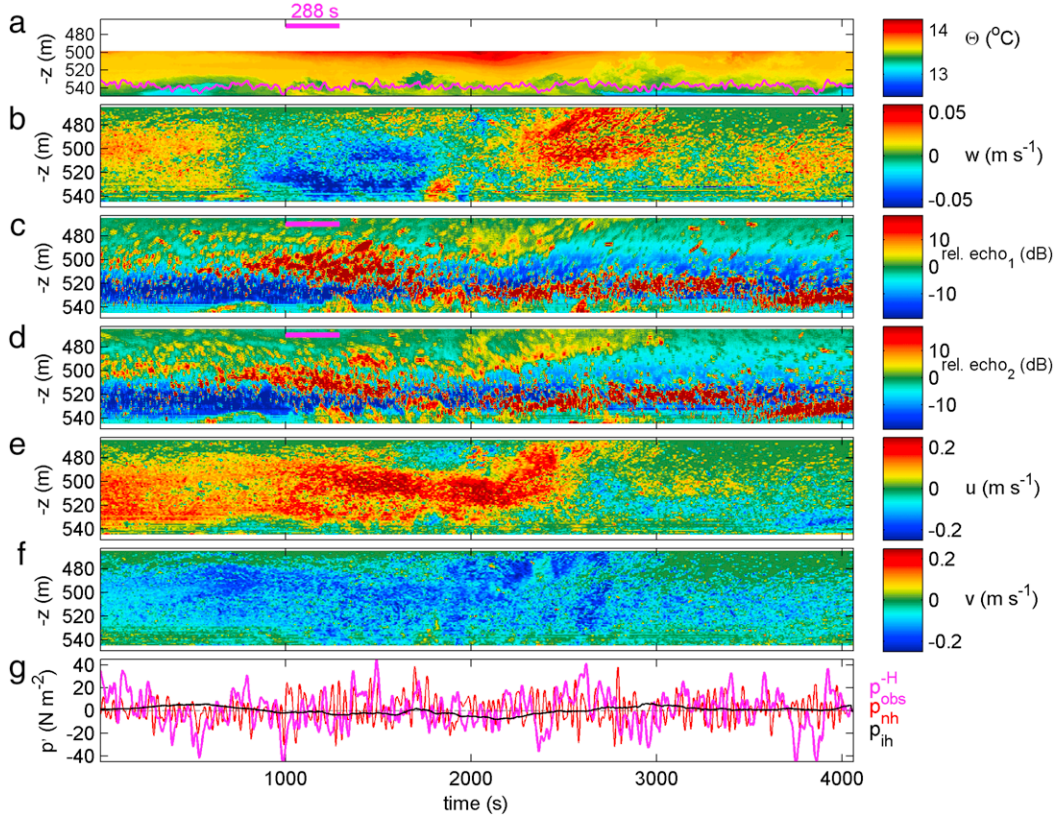

Fig. 7. Additional acoustic current (10 s smoothed data) and pressure (3 s sampled) information to observations in Fig. 6, extending the vertical-range to 85 m above the bottom to include all ADCP-data. (a) Repeat of Fig. 6(a) for reference, without contour lines, but including bottom pressure time series minus its time mean (purple graph, arbitrary scale). (b) Vertical current component. (c) Acoustic echo amplitude of beam 1. (d) Acoustic echo amplitude of beam 2. (e) Cross-slope current component. (f) Along-slope current component. (g) Time series of pressure with reference to their time mean. Observed bottom pressure (purple graph from panel a.) in comparison with estimates of internal hydrostatic pressure (black) and non-hydrostatic pressure (red). (For interpretation of the references to color in this figure legend, the reader is referred to the web version of this article.)

well explain the variance of the observed bottom pressure. The phase is not well explained, which is understandable given the all-sided nature of pressure and the sampling-limitations (of 50 m range of integration of temperature and coarse 10 m^2 horizontally averaged vertical currents measured at 5 m above instead of at the bottom).

4. Discussion and conclusions

The present observations of apparent RTi entraining in stable stratification under internal waves are not uniquely confined to steep slopes, super-critical for internal tides, and some 300 m below the summit of Great Meteor Seamount. They have also been observed in other ocean areas, although mainly in the weaker stratified parts associated with non-linear (internal) wave breaking, indeed above sloping underwater topography.

It seems that the here observed a(de)ccelerations of strong RTi-turbulence in the near-homogeneous layer above, in combination with the internal wave vertical motion variations, can overcome reduced gravity to sufficiently penetrate the stable stratified layer below. Reduced gravity $g' = g\Delta\rho/\rho \approx 2\,g$A is the natural driving force for internal waves in stable-stratified fluids. As the ocean has so much smaller Atwood number A than employed in laboratory experiments, *viz.* $A \sim 10^{-5}$ versus $A \sim O(10^{-3} - 1)$, g' should replace g in considering accelerations to overcome stable stratification. (Olson and Jacobs [5] worked in their laboratory with a launcher capable of accelerations of a few times g experimenting with fluids in which $A = 0.15$–0.21). As the present wave-induced penetration has vertical motion variations of $\Delta w \approx 0.05$ m s^{-1}, the condition for the magnitude of its accelerations is $\Delta w/\Delta t = a_w > -g'$. This is satisfied when $\Delta t < 250$ s, for negative Δw. Such condition and values are observed at the onset of apparent-RTi. This time-variation limit is close to the minimum buoyancy period of 288 s in Figs. 6, 7, or the largest turbulence time-scale of the entrainment-overturns (fingers) observed.

Later in the record however, w becomes positive when isopycnals move upwards whereas the vertical turbulent penetrations continue, creating a more fully turbulent layer touching the bottom. Alternatively, using the above same observed parameter values in Turner's (1968) [14] (and [6]) dependence $w_e/V \sim \mathrm{Ri}^{-1}$ for entrainment velocity across a stable stratified interface, one finds Ri ≈ 0.2 for a vertical scale height of $\Delta z = 10$ m, $V = 0.1$ m s^{-1} and $\Delta\rho = 0.02$ kg m^{-3}. Such a low Ri is a sufficient condition for turbulence exchange, even in the linear stability case [15,16]. Hereby, the small-scale internal wave shear adds positively and sufficiently to the larger-scale internal tide shear. No clear sign of KHi, or of its convective stage, is observed in either temperature or stratification (N) images.

Whatever precise mechanism dominates, the penetrative turbulent near-bottom layer retains a character of stratified turbulence, rather than turbulence creating a purely well-mixed layer. This stratified-turbulence-character may not only be due to a lack of sufficient turbulent kinetic energy, but also to non-negligible potential energy supply of restratification via lateral advection either by large-scale motions or, as is the case here, via small-scale waves. The potential importance of the latter via (self-)advection has been suggested previously [8,41].

As a result, over the course of about half an hour, one large-scale mean buoyancy period, the mid-stage of RTi-penetration can be observed in some detail passing the moored temperature

sensors. Although it is rather rare, being the only clear example in an 18-day (35-tidal periods) time series, the relatively low Atwood number of this natural environment provides some advantage over lab-experiments. The latter reveals such stage only using high-sampling rate observational techniques of duration <1 s (e.g., [3–5]).

For the stable stratified ocean, the observed process of internal-wave-induced RTi may be important as its mixing is expected to be efficient, considering the relatively high vertical density(heat)-flux values. High mixing efficiency is important for any (turbulent) diapycnal transport, whether of heat, suspended sediment or nutrients, and its effects on the marine biology.

From a fluid dynamical viewpoint, the observed tens of meters high penetrative RTi in stable stratification may challenge future modeling and theoretical studies. Specifically, the relative contributions of internal wave acceleration overcoming gravity and self-advection creating free convection need to be tackled. Also, the background conditions leading to entrainment in stable stratification may be precised to understand the importance of interior RTi, with respect to that of the large-scale shear and the small-scale (high-frequency) internal wave motions. Further modeling work is also required on the mixing efficiency of these internal waves breaking above sloping topography in a high $O(10^6)$ Reynolds number environment, like the ocean.

Acknowledgments

Captain and crew of the R/V Pelagia are thanked for the pleasant cooperation during the sea operations. I greatly thank M. Laan and L. Gostiaux for their collaboration in design and construction of NIOZ temperature sensors, hard- and software, besides many discussions. Thoughtful insight was given by L. Maas. The construction of the NIOZ temperature sensors and their deployment during 'LOCO' have been financed in part by NWO, The Netherlands Organization for the advancement of scientific research.

References

[1] D.H. Sharp, An overview of Rayleigh–Taylor instability, Physica D 12 (1984) 3–18.
[2] H.J. Kull, Theory of the Rayleigh–Taylor instability, Phys. Rep. 206 (1991) 197–325.
[3] S.B. Dalziel, Rayleigh–Taylor instability: experiments with image analysis, Dyn. Atmos. Oceans 20 (1993) 127–153.
[4] S.I. Voropayev, Y.D. Afanasyev, G.J.F. van Heijst, Experiments on the evolution of gravitational instability of an overturned, initially stably stratified fluid, Phys. Fluids A 5 (1993) 2461–2466.
[5] D.H. Olson, J.W. Jacobs, Experimental study of Rayleigh–Taylor instability with a complex initial perturbation, Phys. Fluids 21 (2009) 034103.
[6] J.W. Jacobs, S.B. Dalziel, Rayleigh–Taylor instabilities in complex stratifications, J. Fluid Mech. 542 (2005) 251–279.
[7] D.W. Beran, C.G. Little, B.C. Willmarth, Acoustic doppler measurements of vertical velocities in the atmosphere, Nature 230 (1971) 160–162.
[8] I. Orlanski, B.B. Ross, Numerical simulation of the generation and breaking of internal gravity waves, J. Geophys. Res. 78 (1973) 8808–8826.
[9] N.S. Oakey, Determination of the rate of dissipation of turbulent energy from simultaneous temperature and velocity shear microstructure measurements, J. Phys. Oceanogr. 12 (1982) 256–271.
[10] S. Li, H. Li, 2006. Parallel AMR code for compressible MHD and HD equations. T-7, MS B284, Theoretical division, Los Alamos National Laboratory, http://math.lanl.gov/Research/Highlights/amrmhd.shtml.
[11] Y. Matsumoto, M. Hoshino, Onset of turbulence by a Kelvin–Helmholtz vortex, Geophys. Res. Lett. 31 (2004) L02807. http://dx.doi.org/10.1029/2003GL018195.
[12] S.A. Thorpe, A method of producing a shear flow in a stratified fluid, J. Fluid Mech. 32 (1968) 693–704.
[13] M.J. Andrews, S.B. Dalziel, Small Atwood number Rayleigh–Taylor experiments, Philos. Trans. R. Soc. Lond. A 368 (2010) 1663–1679.
[14] J.S. Turner, The influence of molecular diffusivity on turbulent entrainment across a density interface, J. Fluid Mech. 33 (1968) 639–656.
[15] J.W. Miles, On the stability of heterogeneous shear flows, J. Fluid Mech. 10 (1961) 496–508.
[16] L.N. Howard, Note on a paper of John W. Miles, J. Fluid Mech. 10 (1961) 509–512.
[17] G. Holloway, A conjecture relating oceanic internal waves and small-scale processes, Atmos.-Ocean 21 (1983) 107–122.
[18] H.D.I. Abarbanel, D.D. Holm, J.E. Marsden, T. Ratiu, Richardson number criterion for the nonlinear stability of three-dimensional stratified flow, Phys. Rev. Lett. 52 (1984) 2352–2355.
[19] A.J. Majda, M. Shefter, The instability of stratified flows at large Richardson numbers, Proc. Natl. Acad. Sci. USA 95 (1998) 7850–7853.
[20] J.D. Woods, Wave-induced shear instability in the summer thermocline, J. Fluid Mech. 32 (1968) 791–800.
[21] S.A. Thorpe, A.J. Hall, C. Taylor, J. Allen, Billows in Loch Ness, Deep-Sea Res. 24 (1977) 371–379.
[22] H.E. Seim, M.C. Gregg, Detailed observation of a naturally occurring shear instability, J. Geophys. Res. 99 (1994) 10049–10073.
[23] H. Li, H. Yamazaki, Observations of a Kelvin–Helmholtz billow in the ocean, J. Oceanogr. 57 (2001) 709–721.
[24] J.N. Moum, D.M. Farmer, W.D. Smyth, L. Armi, S. Vagle, Structure and generation of turbulence at interfaces strained by internal solitary waves propagating shoreward over the continental shelf, J. Phys. Oceanogr. 33 (2003) 2093–2122.
[25] H. van Haren, L. Gostiaux, A deep-ocean Kelvin–Helmholtz billow train, Geophys. Res. Lett. 37 (2010) L03605. http://dx.doi.org/10.1029/2009GL041890.
[26] H. van Haren, M. Laan, D.-J. Buijsman, L. Gostiaux, M.G. Smit, E. Keijzer, NIOZ3: independent temperature sensors sampling yearlong data at a rate of 1 Hz, IEEE J. Ocean. Eng. 34 (2009) 315–322.
[27] H. van Haren, Bottom-pressure observations of deep-sea internal hydrostatic and non-hydrostatic motions, J. Fluid Mech. 714 (2013) 591–611.
[28] RDI. 1996. A practical primer. San Diego: Teledyne-RDI, San Diego, CA, 32 pp.
[29] T.K. Stanton, P.H. Wiebe, D. Chu, L. Goodman, Acoustic characterization and discrimination of marine zooplankton and turbulence, ICES J. Mar. Sci. 51 (1994) 469–479.
[30] H. van Haren, L. Gostiaux, Detailed internal wave mixing above a deep-ocean slope, J. Mar. Res. 70 (2012) 173–197.
[31] T.J. McDougall, R. Feistel, F.J. Millero, D.R. Jackett, D.G. Wright, B.A. King, G.M. Marion, C.-T.A. Chen, P. Spitzer, Calculation of the Thermodynamic Properties of Seawater, Global Ship-based Repeat Hydrography Manual. IOCCP Report 14, ICPO Publication Series 134, U.N.E.S.C.O, Paris, F, 2009.
[32] S.A. Thorpe, Turbulence and mixing in a Scottish loch, Philos. Trans. R. Soc. Lond. Ser. A 286 (1977) 125–181.
[33] S.A. Thorpe, Current and temperature variability on the continental slope, Philos. Trans. R. Soc. Lond. Ser. A 323 (1987) 471–517.
[34] T.M. Dillon, Vertical overturns: a comparison of Thorpe and Ozmidov length scales, J. Geophys. Res. 87 (1982) 9601–9613.
[35] J.C. Wesson, M.C. Gregg, Mixing at Camarinal Sill in the Strait of Gibraltar, J. Geophys. Res. 99 (1994) 9847–9878.
[36] T.R. Osborn, Estimates of the local rate of vertical diffusion from dissipation measurements, J. Phys. Oceanogr. 10 (1980) 83–89.
[37] K. Stansfield, C. Garrett, R. Dewey, The probability distribution of the Thorpe displacement within overturns in Juan de Fuca Strait, J. Phys. Oceanogr. 31 (2001) 3421–3434.
[38] L. St. Laurent, R.W. Schmitt, The contribution of salt fingers to vertical mixing in the North Atlantic tracer release experiment, J. Phys. Oceanogr. 29 (1999) 1404–1424.
[39] H. van Haren, Stratified turbulence and small-scale internal waves above deep-ocean topography, Phys. Fluids 25 (2013) 106604. http://dx.doi.org/10.1063/1.4826888.
[40] S.C. Webb, Broadband seismology and noise under the ocean, Rev. Geophys. 36 (1998) 105–142.
[41] J.S. Frederiksen, Interactions of nonlinear internal gravity-waves and turbulence, Ann. Geophys. 2 (1984) 421–432.